

Numerical investigation of Typhoon Kai-tak (1213) using a mesoscale coupled WRF-ROMS model



Zhiyuan Wu^{a,b,c,d}, Changbo Jiang^{a,b,*}, Bin Deng^{a,b}, Jie Chen^{a,b}, Yuannan Long^{a,b}, Ke Qu^{a,b}, Xiaojian Liu^d

^a School of Hydraulic Engineering, Changsha University of Science & Technology, Changsha, 410114, China

^b Key Laboratory of Water-Sediment Sciences and Water Disaster Prevention of Hunan Province, Changsha, 410114, China

^c School for Marine Science and Technology, University of Massachusetts Dartmouth, New Bedford, MA, 02744, USA

^d Key Laboratory of the Pearl River Estuarine Dynamics and Associated Process Regulation, Ministry of Water Resources, Guangzhou, 510611, China

ARTICLE INFO

Keywords:

Storm surge
Typhoon
Coupled atmosphere-ocean model
Sea-air interaction
WRF
ROMS

ABSTRACT

The Typhoon Kai-tak that occurred in August 2012 produced strong winds, heavy rain, extreme wave, and storm surge, which also had a significant impact on the coastal areas of China and Vietnam. Studying the formation and tracking the movement mechanism of this typhoon will help reduce future coastal disasters, as well as have important scientific significance. The impact of a typhoon creates strong mass transport and energy exchange between the atmosphere and the ocean which produces a strong interaction between the wind field and the flow field. A coupled atmosphere-ocean model in the South China Sea was established based on the mesoscale atmospheric model WRF and the regional ocean model ROMS. Typhoon Kai-tak was simulated using this model. The simulation results show that the coupled WRF-ROMS model indicate high simulation accuracy with respect of storm surge in the South China Sea under the influence of Typhoon Kai-tak. The simulation results also reveal the temporal and spatial distribution of Typhoon Kai-tak's field, storm surge, and wind-induced flow fields. The spatial asymmetry and time lag in the spatial-temporal distribution of sea surface temperature during Typhoon Kai-tak have been discussed. The heat exchange at the air-sea interface was very strong under the influence of Typhoon Kai-tak, and the latent heat generated by water vapor evaporation plays a dominant role in the heat exchange at the air-sea interface, which shows that the heat carried by the vaporization of the sea surface is one of the important factors for the decrease of sea temperature under the influence of a typhoon.

1. Introduction

The Northwest Pacific and the South China Sea region are the birthplaces of most monsoons and typhoons and are an important channel for the generation and transmission of water vapor (Chia and Ropelewski, 2002; Wang et al., 2007; Sun et al., 2017; Wu et al., 2018). The Northwest Pacific plays a major role in regulating interdecadal and long-term changes in climate (Hu et al., 2015; Xie et al., 2016). China is the region with the largest number of typhoons and the most destructive power affected by typhoons in the world (Liu et al., 2009). China is also one of the countries with the most serious marine and meteorological disasters. In the context of global warming, the probability of occurrence of extreme weather events has continuously increased and have caused a large degree of impact on the offshore areas (Wang et al., 2010).

Compared with large-scale phenomena such as global climate

change, small- and medium-scale phenomena such as typhoons and thunderstorms have an even greater impact on people's production and life (Yang et al., 2018). Typhoons and hurricanes present some of the greatest threats to life and damage to property (Mooney et al., 2019). The influence of a typhoon on a region is often not only a heavy wind disaster. At the same time, the heavy rain, extreme waves, storm surges and beach erosion (Yang et al., 2015; Ge et al., 2017; Jiang et al., 2017; Mei et al., 2018) that are produced will also have a huge impact on the region, which will result in the formation of a typhoon disaster chain (Lee, 2006; Wu et al., 2019). Therefore, studying the movement mechanism of typhoon, accurately forecasting the influence of typhoon and reducing storm surge disasters have important social value for the protection of national economic development and human and property safety.

The current problem of marine environmental forecasting is attempting to predict the impact of such extreme weather. Due to the

* Corresponding author. School of Hydraulic Engineering, Changsha University of Science & Technology, Changsha, 410114, China.

E-mail address: jiangchb@csust.edu.cn (C. Jiang).

relative lack of marine data, research on such issues mainly relies on numerical simulations. Scholars have developed a variety of models for forecasting storm surge. As early as 1972, Jelenski developed the SPLASH model followed by the SLOSH model (Jelenski et al., 1992), which was widely used in storm surge simulation in seas, lakes, and on land (Forbes et al., 2014; Hu et al., 2015; Neumann et al., 2015). Blumberg and Mellor (1987) developed the POM model to simulate large-scale ocean and coastal water levels, and flow field changes (Xie et al., 2004; Li et al., 2013). Many ocean models have been developed and used for the simulation of storm surges, such as the ECOM model (Di et al., 2011; Blumberg et al., 2015), ROMS model (Li et al., 2006; You et al., 2010), CH3D-IMS model (Sheng et al., 2010), CEST model (Zhang et al., 2013), SELFE model (Zhang and Baptista, 2008), Delft3D model (Vu and Lam, 2005), ADCIRC model (Mattocks and Forbes, 2008; Sebastian et al., 2014) and FVCOM model (Weisberg and Zheng, 2006; Rego and Li, 2010; Chen et al., 2018). They have achieved very good results and laid the foundation for understanding the dynamic mechanism of storm surges.

There is a strong mass transport, energy exchange and interaction between the atmosphere and the ocean during a typhoon (Black et al., 2007). The physics fields such as the wind field, flow field, and wave field influence each other and restrict each other. The forcing effect of the atmosphere on the ocean mainly includes wind stress, pressure, heat flux, and solar radiation on the sea surface. Additionally, the upper ocean responds to the atmospheric effects, and its response results in atmospheric dynamics processes. The role of the oceans in the atmosphere mainly includes two aspects. First, changes in the sea surface temperature (SST) lead to changes in the sea surface heat flux, which affects the movement of the atmosphere; second, changes in the sea surface flow field cause the wind stress at the bottom of the atmosphere to change, and affect the atmosphere movement structure (Liu et al., 2010).

During the evolution of storm surge induced by a typhoon, there are many factors, including the influence of different spatial and temporal scales and different physical factors, such as wind speed, air pressure, runoff, wave, and astronomical tide and others, which makes it difficult to accurately simulate storm surges (Mori et al., 2014; Takagi et al., 2017; Yin et al., 2017; Wang et al., 2018). The development of a coupled atmospheric and ocean model had significant effects on improving the accuracy of numerical prediction (Liu et al., 2015; Yang and Haas, 2015; Gronholz et al., 2017). The establishment of a coupled atmosphere and ocean model is an effective method to solve this problem. Mesoscale meteorological models such as the MM5 model (Wang et al., 2017) or the WRF model (Warner et al., 2010; Zambon et al., 2014; Pattanayak et al., 2016; Lakshmi et al., 2017) were used to provide high accuracy and precision of wind and pressure field for the ocean model. By establishing a coupled atmosphere and ocean model, the sea-air interface information exchange was achieved, and the simulation accuracy of storm surge was improved.

The coupled WRF-ROMS model in the South China Sea has been established using the model coupling toolkit (MCT), the mesoscale atmospheric model WRF and the regional ocean model ROMS based on the COAWST modeling system in this study. Typhoon Kai-tak and storm surge were simulated based on this coupled model. The characteristics of atmospheric motion and flow movement in the South China Sea under the influence of typhoon were calculated. The temporal and spatial distribution characteristics of the storm surge in the South China Sea were analyzed in this study.

2. Methodology and data

2.1. Numerical tools

2.1.1. WRF: atmospheric module

The WRF (Weather Research and Forecasting) model is the latest generation of mesoscale meteorological model jointly developed by

research institutes such as the NCAR (National Center for Atmospheric Research) and NCEP (National Centers for Environmental Prediction). Version V1.0 of the WRF model was released in November 2000, and the version 3.9.1 released on August 2017 have been used to simulate typhoon in this study. The WRF model can be used to simulate climate change, atmospheric motion, and air quality at different scales, such as global and regional scales. It can also be used for simulation of typhoon or hurricane, and atmosphere and ocean interaction. The WRF model has a wide range of applications in different field and become the most popular mesoscale atmosphere model now.

The WRF model includes two different frameworks, ARW (the Advanced Research WRF) and NMM (the Non-hydrostatic Mesoscale Model), which maintained and developed by the NCAR and NCEP respectively. The ARW framework in the WRF model is used in this study. This model adopts a fully compressible non-hydrostatic model with Arakawa C grid in the horizontal direction and terrain-following quality coordinates in the vertical direction (Laprise, 1992).

2.1.2. ROMS: oceanic module

The Regional Ocean Model System (ROMS) is one of the most advanced ocean model systems in the world. The ROMS model adopts the Stretched Terrain Following Coordinates in the vertical direction, which can properly describe the influence of the topography. In the vertical direction, non-equal-scale stratification can be used, which can get higher simulation accuracy at the thermocline and the bottom boundary layer.

The momentum equations of ROMS model are as shown in Eqs. (1)–(3) (Haidvogel et al., 2008):

$$\begin{aligned} & \frac{\partial(H_z u)}{\partial t} + \frac{\partial(u H_z u)}{\partial x} + \frac{\partial(v H_z u)}{\partial y} + \frac{\partial(w H_z u)}{\partial s} - f H_z v \\ &= -\frac{H_z}{\rho_0} \frac{\partial p}{\partial x} - H_z g \frac{\partial \eta}{\partial x} - \frac{\partial}{\partial s} \left(\bar{u}' w' - \frac{v}{H_z} \frac{\partial u}{\partial s} \right) - \frac{\partial(H_z S_{xx})}{\partial x} - \frac{\partial(H_z S_{xy})}{\partial y} + \frac{\partial S_{px}}{\partial s} \end{aligned} \quad (1)$$

$$\begin{aligned} & \frac{\partial(H_z v)}{\partial t} + \frac{\partial(u H_z v)}{\partial x} + \frac{\partial(v H_z v)}{\partial y} + \frac{\partial(w H_z v)}{\partial s} - f H_z u \\ &= -\frac{H_z}{\rho_0} \frac{\partial p}{\partial y} - H_z g \frac{\partial \eta}{\partial y} - \frac{\partial}{\partial s} \left(\bar{v}' w' - \frac{v}{H_z} \frac{\partial v}{\partial s} \right) - \frac{\partial(H_z S_{yx})}{\partial x} - \frac{\partial(H_z S_{yy})}{\partial y} + \frac{\partial S_{py}}{\partial s} \end{aligned} \quad (2)$$

$$-\frac{1}{\rho_0} \frac{\partial p}{\partial s} - \frac{g}{\rho_0} H_z \rho = 0 \quad (3)$$

The continuity equation is:

$$\frac{\partial \eta}{\partial t} + \frac{\partial(H_z u)}{\partial x} + \frac{\partial(H_z v)}{\partial y} + \frac{\partial(H_z w)}{\partial s} = 0 \quad (4)$$

The convection-diffusion equation is:

$$\begin{aligned} & \frac{\partial(H_z C)}{\partial t} + \frac{\partial(u H_z C)}{\partial x} + \frac{\partial(v H_z C)}{\partial y} + \frac{\partial(w H_z C)}{\partial s} = -\frac{\partial}{\partial s} \left(c' w' - \frac{v_\theta}{H_z} \frac{\partial C}{\partial s} \right) \\ &+ C_{source} \end{aligned} \quad (5)$$

The water state equation is:

$$\rho = f(C) \quad (6)$$

In the above Eqs. (4) and (5), u , v and w respectively represent the flow velocity in the three directions of x , y and z , and in the vertical σ coordinate, $s = (z - \eta)/(h + \eta)$, $-1 < s < 0$.

2.1.3. Coupled WRF-ROMS model

In order to effectively simulate the ocean dynamic process under the influence of typhoon, the mesoscale atmospheric model WRF and the regional ocean model ROMS was coupled based on the model coupling toolkit (MCT, Craig et al., 2005), and the interaction between the ocean and typhoon has been considered in this study. A coupled atmosphere and ocean model in the South China Sea has been established. The schematic diagram of the coupled model system is shown in Fig. 1 based on COAWST modeling system (Warner et al., 2008). It can be seen from the figure that there is a two-way coupling between the WRF

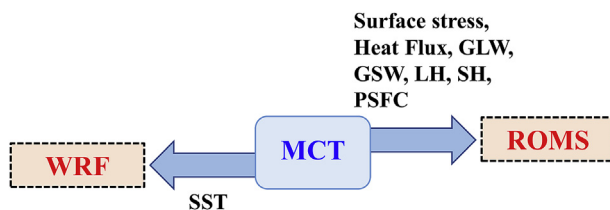


Fig. 1. Variables exchanged in the coupled WRF-ROMS model.

and ROMS model, that is, the surface stress, net heat fluxes, and sensible heat flux, latent heat flux, shortwave radiation flux, and longwave radiation flux calculated by WRF and delivered to ROMS through the MCT coupler. While, the sea surface temperature (SST) calculated by ROMS is feedback to the WRF through the MCT coupler.

In summary, the sea surface temperature can affect the intensity of the typhoon is an opinion easy to understand. The asymmetric distribution of sea surface temperature affects the thermal radiation process and heat flux exchange between the ocean and the atmosphere, thus affecting the water vapor exchange process. The result of these dynamic processes is that the intensity of the typhoon changes. For example, if the ocean is warmer and the sea surface temperature is higher, during the typhoon movement, the typhoon can get more energy from the ocean, and at the same time strengthen the exchange of water vapor at the sea-air interface, resulting in an increase in the intensity of the typhoon, which will lead to an increase in storm surge.

2.2. Basic data and initial and boundary conditions

The shoreline data comes from the Global Self-consistent, Hierarchical, High-resolution Shorelines (GSHHS) provided by the National Geophysical Data Center (NGDC). The dataset provides 1:250000 worldwide coastline data (see Fig. 2). The depth data used in this model comes from the 1-Minute Gridded Global Relief Data Collection (ETOPO1) provided by the NGDC. The dataset has a grid resolution of 1 min. The coverage range is between 90 °S to 90 °N and 180 °W to 180 °E.

The initial field and side boundary conditions of the WRF model are taken from the NCEP/NCAR reanalysis FNL data. The reanalysis FNL data provided by the NCEP/NCAR uses the GRIB format and contains 26 non-uniformly distributed pressure data from 1000 hPa to 10 hPa. The time range is updated from August 1999 to date. The data interval is 6 h, which means that the daily data includes 00:00, 06:00, 12:00, and 18:00 in one day. The spatial resolution of the data is 1.0° × 1.0°.

The harmonic constants of the ROMS model are derived from the

OTIS model provided from Oregon State University, which has two types, the TPXO global and the various region ocean area type. The calculation region is the South China Sea in this paper, so according to the accuracy, the China Seas and Indonesia 2016 module data in the regional type with higher spatial resolution is selected (<http://volkov.oce.orst.edu/tides/YS.html>). The spatial resolution of this data is 1/30°, with a total of 901 × 1201 grid nodes, and the data is updated to 2016. The data was equated with satellite altimeter data from satellite altimeters such as TOPEX/Poseidon, Jason-1, Jason-2 and tide stations.

2.3. Model configuration

The coupled WRF-ROMS model was used to simulate Typhoon Kai-tak (1213). The simulation time includes the entire process of development and movement of Kai-tak in the South China Sea region (from 2012 to 08-15 00:00 to 2012-08-18 06:00). The simulation domains are the South China Sea and the near region as shown in Fig. 3. The WRF parent domain is from 0°N, 100°E to 32°N, 132.5°E, the WRF child domain is from 12°N, 103°E to 26°N, 131°E, the ROMS parent domain is from 3°N, 105°E to 28°N, 131.5°E, and the ROMS child domain is from 12.5°N, 105.5°E to 24°N, 117°E. The yellow and blue wireframes represent the parent and child simulation domains of the WRF and ROMS, respectively.

The physical and parameterization schemes for Typhoon Kai-tak in the WRF are as follows: the grid resolution in horizontal direction using a two-way nesting grid of 15 km and 5 km, 35 layers has been taken in the vertical direction, and the maximum top pressure recommended 2000Pa. The WSM6 parameterization scheme and Kain-Fritsch scheme has been selected for the microphysical parameterization schemes and cumulus parameterization schemes, respectively, and the YSU scheme has been used for the boundary layer scheme in the WRF model. The configuration of these parameterization schemes refers from some results of previous scholars (Chen et al., 2015; Islam et al., 2015). The initial conditions are provided by the Global Forecast Model (GFS, FNL data) of the NCEP, which has a time accuracy of 6 h and a spatial accuracy of 1°. The D1 model (parent model) outputs the results every 180 min, and the D2 model (child model) outputs the results every 60 min.

The ocean model ROMS uses two-way nesting grids with 170 × 170 nodes (parent grid) and 225 × 240 nodes (child grid). The grid size between parent grid and child grid is 3:1, which are 15 km × 15 km and 5 km × 5 km, respectively. The parent model encompasses the entire South China Sea and nearby sea regions, and the child model mainly includes the central and north of the South China Sea, as shown in Fig. 3. The vertical layer of the double grid is 16 layers, and the vertical

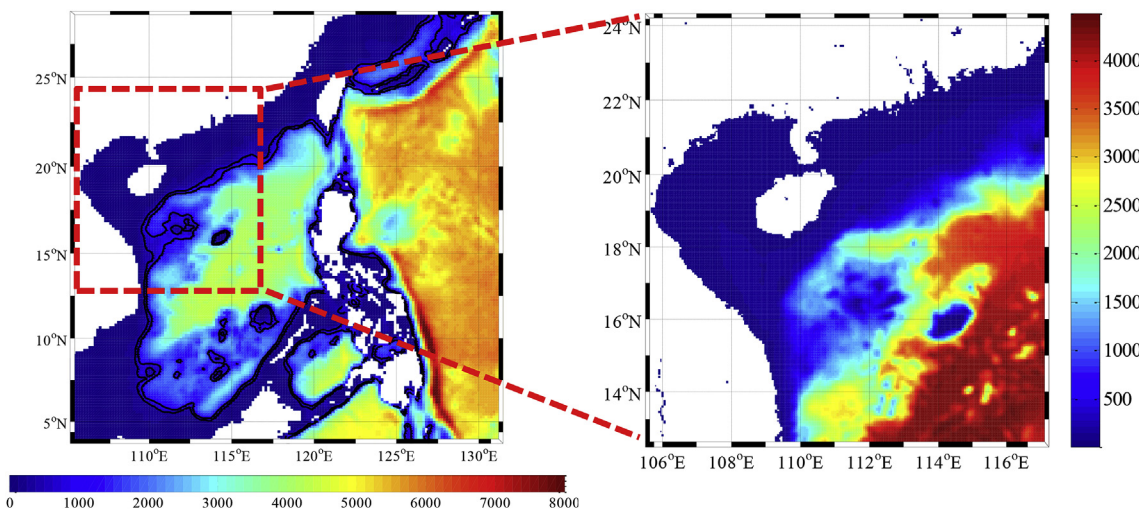


Fig. 2. The topography of the South China sea (unit: m).

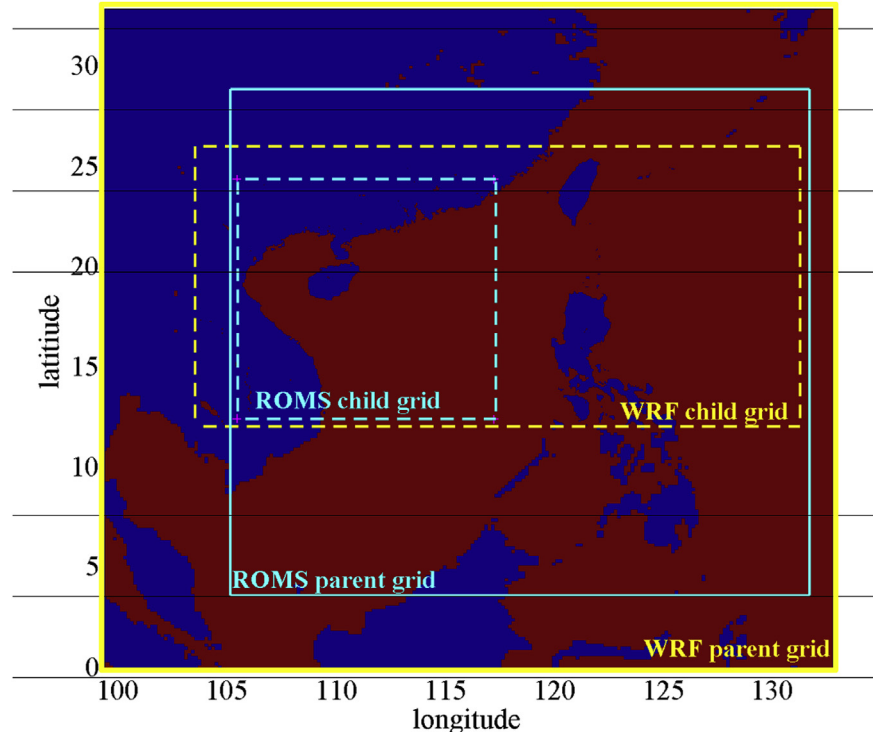


Fig. 3. The simulation domain of the coupled WRF-ROMS model in the South China Sea.

coordinate stretching parameters $\text{THETA_S} = 5.0$, $\text{THETA_B} = 0.4$, that is, the sea surface and bottom layer are improved resolution.

In this study, the atmospheric model has a spatial extent that covers most of the continental South China, South China Sea, Thailand Gulf, Malay Archipelago and Philippine Islands. The atmospheric grid is large enough to provide surface forcing for the ocean model, but the ocean model grids are rotated and with differing cell sizes. The interpolation is required to transfer data between these grids. To allow the models to exchange data fields on different grids we use the Spherical Coordinate Remapping Interpolation Package (SCRIP; Jones, 1998) to compute interpolation weights. The weights are computed as a pre-processing step. They are read in during initialization and used in the sparse matrix interpolation as described in Warner et al. (2008). Currently, we use the nearest neighbor method to compute the weights.

In the ROMS model, as shown in Fig. 3, the east, west, south, and north boundaries of the parent model are all set as open boundaries. The harmonic constants for the eight main tidal of M2, S2, N2, K2, K1, O1, P1, and Q1 obtained from the China Seas and Indonesia 2016 scheme in OTIS. According to the mesh division of the ROMS model, the value of the open boundary point in the model is interpolated by the OSU Tidal Prediction Software (OTPS), and the water level forecast value is obtained through the `t_predict` function, and the obtained water level is used as the open boundary of the ROMS model to drive. The west and north boundaries of the child model are set as closed boundary, and the boundary conditions on the south and east are provided by the parent model. The water level forecast in the parent model is calculated according to the following formula.

$$\zeta = \sum_{i=1}^n f_i H_i \cos(\omega_i t + v_{0i} + u_i - g_i) \quad (7)$$

Where, ζ is the water level, H_i , g_i , ω_i respectively represents the amplitude, the late angle and the angular velocity of the i -th component tide, f_i is the intersection point factor of the tidal component, u_i is the correction angle of the tidal point intersection, and v_{0i} is the astronomical initial phase of the tidal range. The mid-bottom friction coefficient is taken as 0.0015 and the horizontal mixing coefficient is taken

as 0.1 in this study.

The coupled WRF-ROMS model simulate start at 2012-08-15 00:00 (UTC) and ended at 2012-08-18 06:00 (UTC), for a total of 78 h, including entering processes of landing and leaving of Typhoon Kai-tak in the South China Sea. The time step of the atmosphere model WRF is set to 60 s, and the timestep of the parent and child ocean model ROMS is set to 60 s and 20 s, respectively; the time step of the MCT synchronization is set to 600 s.

2.4. Selection of typhoon

Typhoon Kai-tak (201213) formed a tropical depression in the eastern sea of the Philippines on the evening of August 12, 2012. It reached the southeast of Taiwan (16.9°N , 127.8°E) at about 08:00 on the 13th and continued to strengthen. The maximum wind speed reached 18 m/s or more, and the minimum air pressure was 998 hPa. It moved northwestward at a speed of about 10 km/h and gradually approached the southern coast of Taiwan. The track of Typhoon Kai-tak is shown in Fig. 4.

At 05:00 on August 16, 2012, it strengthened to typhoon level over the north of the South China Sea. At 06:00, the center of typhoon was in the south of Zhanjiang, Guangdong Province (18.7°N , 118.2°E). The maximum wind speed near the center was more than 33 m/s, and the minimum pressure in the center is 975 hPa. It made landfall on Zhanjiang in Guangdong Province at approximately 12:30 on August 17th. At the time of landing, the maximum wind speed near the center was 38 m/s, and the minimum pressure in the center was 968 hPa. At 21:30 on the 17th, it landed again on the China-Vietnam coast and began to weaken and gradually dissipated on the 18th. The Typhoon Kai-tak caused heavy rainfall in most parts of southern China and caused floods and other disasters, leading to serious losses in the affected areas.

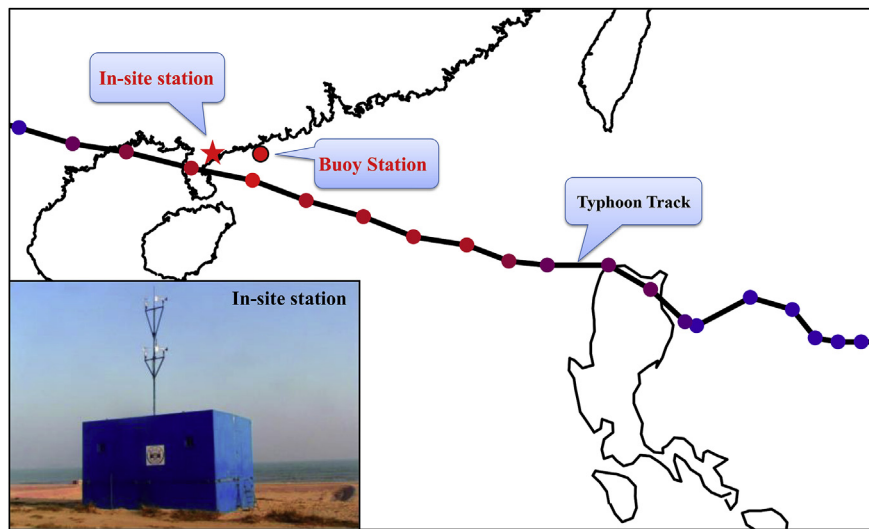


Fig. 4. The track of Typhoon Kai-tak (1213) and the buoy station and in-site station.

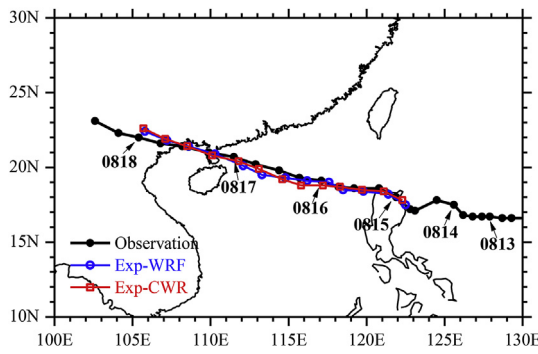


Fig. 5. The typhoon track in different simulation experiments.

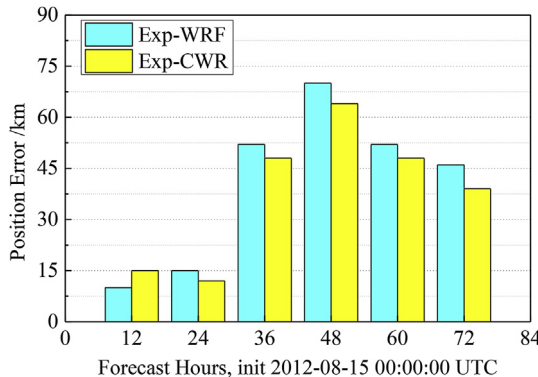


Fig. 6. Comparison of typhoon track errors in two experiments at different time.

3. Model validation

3.1. Typhoon track

Fig. 5 shows the track of Typhoon Kai-tak in two simulation experiments, one uses only the atmospheric model WRF (Exp-WRF) and the other the coupled WRF-ROMS model (Exp-CWR). From the simulation results, the typhoon tracks obtained under the two experiments are similar and correlate with the measured results. However, starting at 00:00 on the 16th, the typhoon moving speed in the simulations of both experiments are slower than the measured results. At 00:00 on the 17th, it was actually observed that the typhoon center had landed, and

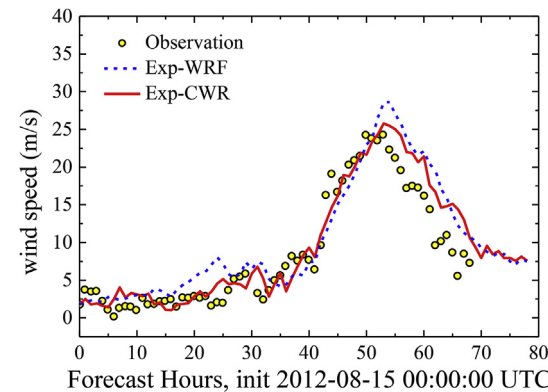


Fig. 7. Comparison of wind speed between two simulation experiments and observation.

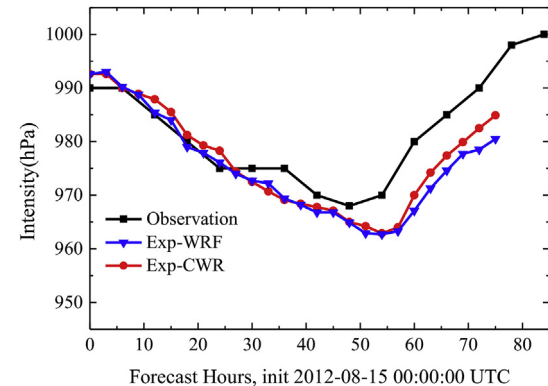


Fig. 8. Comparison of sea level pressure between two simulation experiments and observation.

the numerical calculation results indicated a 3–6 h delay compared to the actual observations.

The typhoon track difference between the measured results and the two simulation experiments has been shown in Fig. 6. It can be seen from the figure that the track error is small in the early stage of the typhoon, that is, from 00:00 on the 15th to 00:00 on the 16th. The path error obtained by the two experiments is within 15 km. Once the typhoon moved to the north and center of the South China Sea, the typhoon speed slowed in the two simulation results, which lead to more

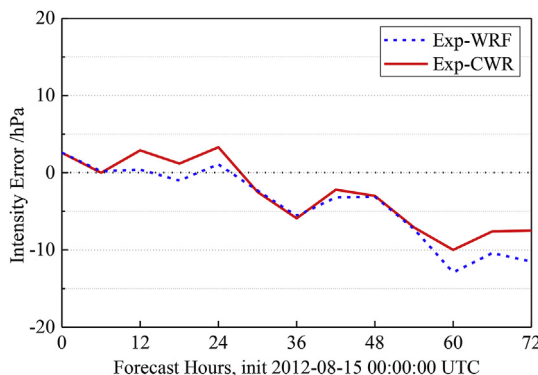


Fig. 9. Comparison of pressure difference between two simulation experiments and observation (simulation value minus observation value).

simulated error. The maximum simulation track error exceeded 60 km. However, the simulation results of the typhoon track for the Kai-tak is somewhat consistent with the measured results. The difference in time and the resulting track error can be accepted by the numerical simulation.

3.2. Typhoon intensity and strength

The comparison of calculated and observed wind speed at the observation station (in Fig. 4) has been shown in Fig. 7, which compares the wind speed simulation results for the two different experiments. It can be seen from Fig. 7 that in the coupled WRF-ROMS model (Exp-

CWR), the trend of the typhoon wind speed at the observation point is equivalent to the calculated value. In the period of maximum and decreasing wind speed, the calculated value of wind speed by the coupled model (Exp-CWR) is reduced relative to the Exp-WRF scheme (only WRF model), and the calculation result is closer to the observation value. The WRF only case (blue line) contains larger errors than the coupled WRF-ROMS case (red line), which was not a strong attempt to correct the track and intensity with strong data nudging, rather a commitment to investigate the variability that develops as additional physics are activated. The coupled WRF-ROMS case allowed SST from ROMS to affect the atmosphere, which then created a slight adjustment of the track. The coupled model can improve the problem of larger wind speed simulated by the WRF model.

Fig. 8 shows the change of the minimum sea level pressure (SLP) in the typhoon center over time for the two different experiments. It can be seen from the figure that during the typhoon movement, the minimum SLP in the typhoon center continued to decrease. In the 54th hour (2012-08-17 06:00:00 UTC) sea level pressure reached the lowest level, approaching 960 hPa. Since then, the intensity decreased and the minimum SLP increased due to the landing of the typhoon. As can be seen from the figure, the curve slope of the rising phase is larger during the typhoon processes over time, which indicates the typhoon pressure recovery rate after landing is greater than the typhoon pressure when the typhoon moves on the sea region.

The SLP difference comparison of the two simulation experiments and the observation has been shown in Fig. 9. It can be found that the value of the simulation result minus the observation result is negative after the 24 h. This indicates that the sea level pressure of the simulation result is less than the actual pressure, showing that the intensity of

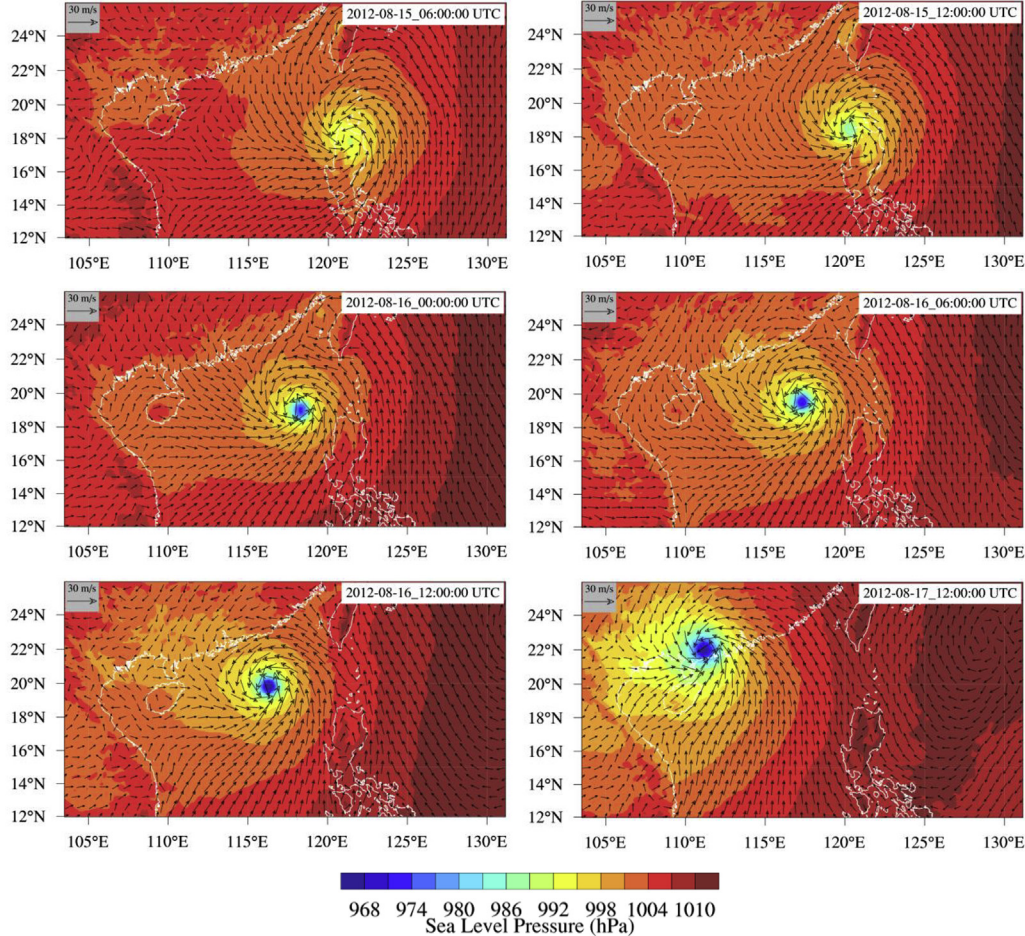


Fig. 10. Spatial distribution of wind field and pressure field influenced by Typhoon Kai-tak.

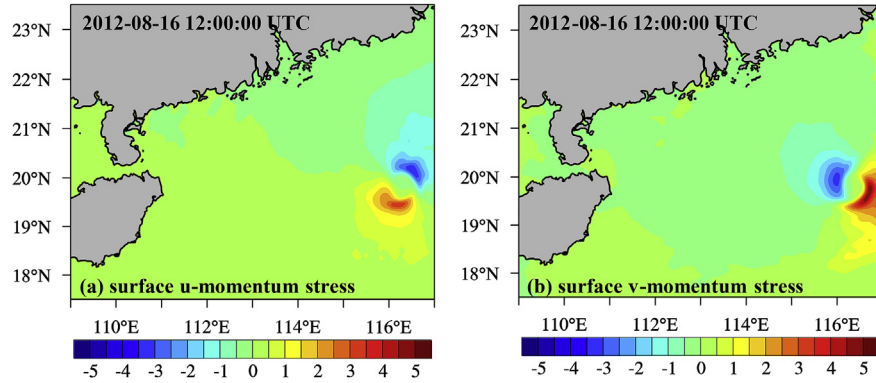


Fig. 11. Spatial distribution of surface stress influenced by Typhoon Kai-tak (unit: N/m^2).

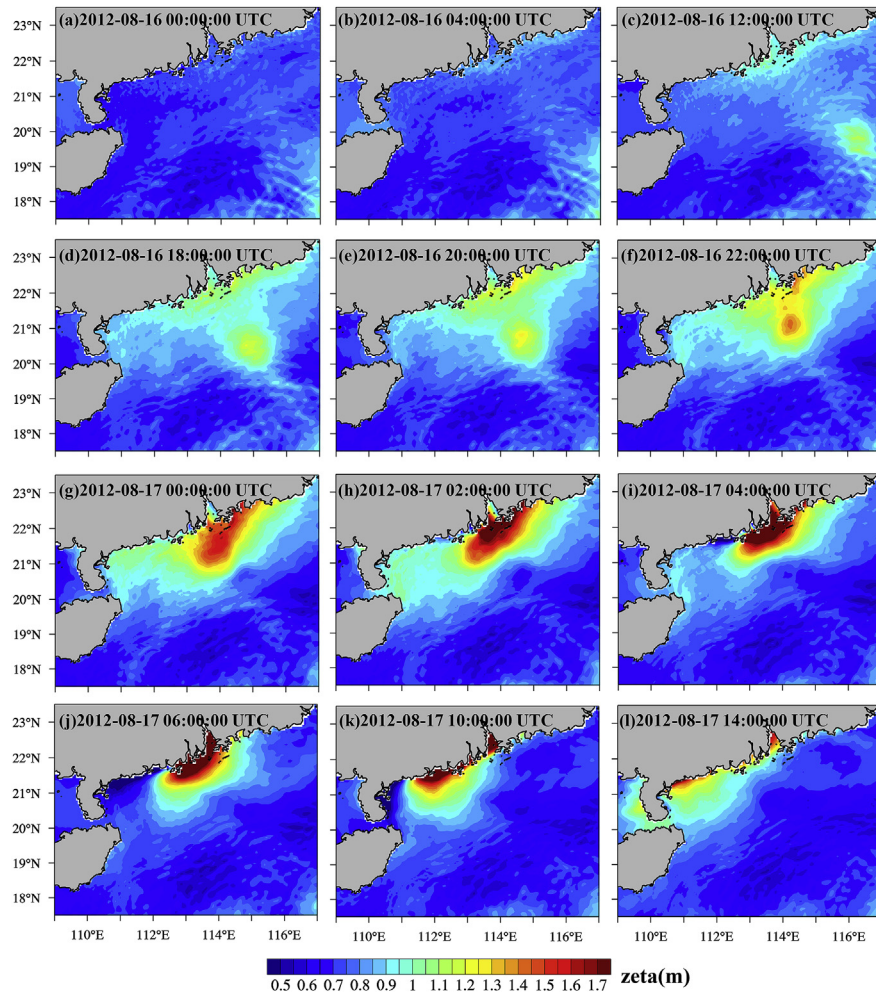


Fig. 12. Spatial distribution of water level influenced by Typhoon Kai-tak.

simulation result is greater than the observation. This is the same as the simulation results of the typhoon wind speed. Because the moving speed of typhoon in the simulation model is slower, the simulated intensity is also stronger than the observation.

Comparing the results of Exp-CWR, Exp-WRF, and the observation, it can be seen that under the two different experimental scenarios, the development trend of typhoon intensity error is quiet. In the later stage of the typhoon process, the simulation error slightly increases, but the difference between the simulation value of the SLP and the observation value is at a range of 10 hPa. The simulation results of the coupled scheme (Exp-CWR) are better than those of the WRF only scheme (Exp-

WRF), and they more accurately reflect the development and evolution of the typhoon sea level and dynamic processes, and can simulate the intensity and strength of the Typhoon Kai-tak.

4. Results and discussions

4.1. Wind and pressure field

Fig. 10 shows the spatial distribution of wind field at 10m and pressure field obtained by the coupled WRF-ROMS model during the influence of Typhoon Kai-tak. It records that Kai-tak moved from the

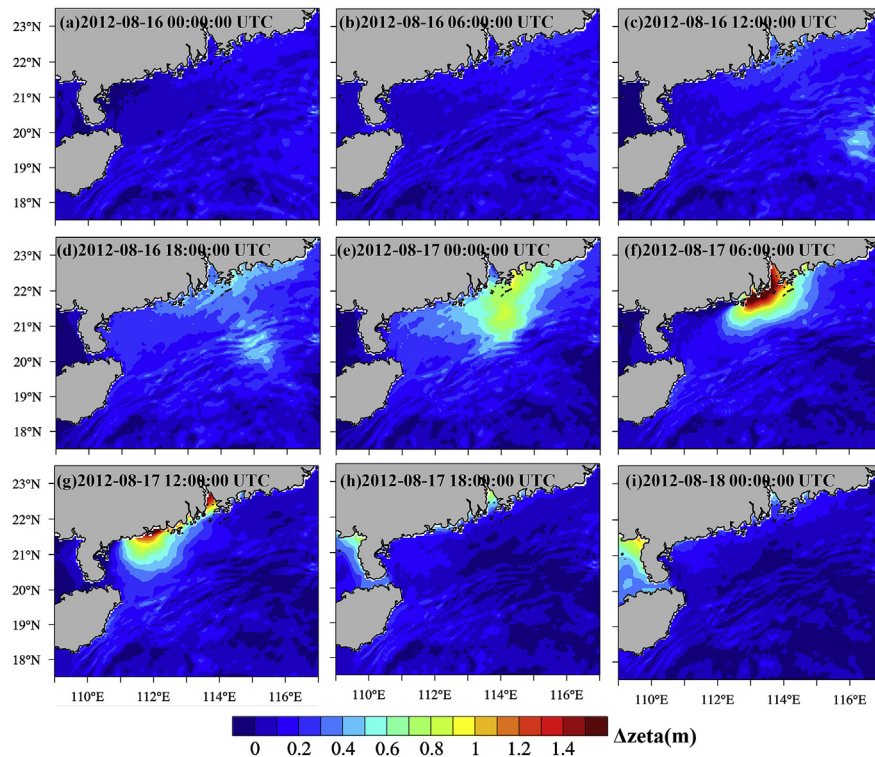


Fig. 13. Spatial distribution of storm surge level influenced by Typhoon Kai-tak.
(start at 2012-08-15 00:00:00 UTC).

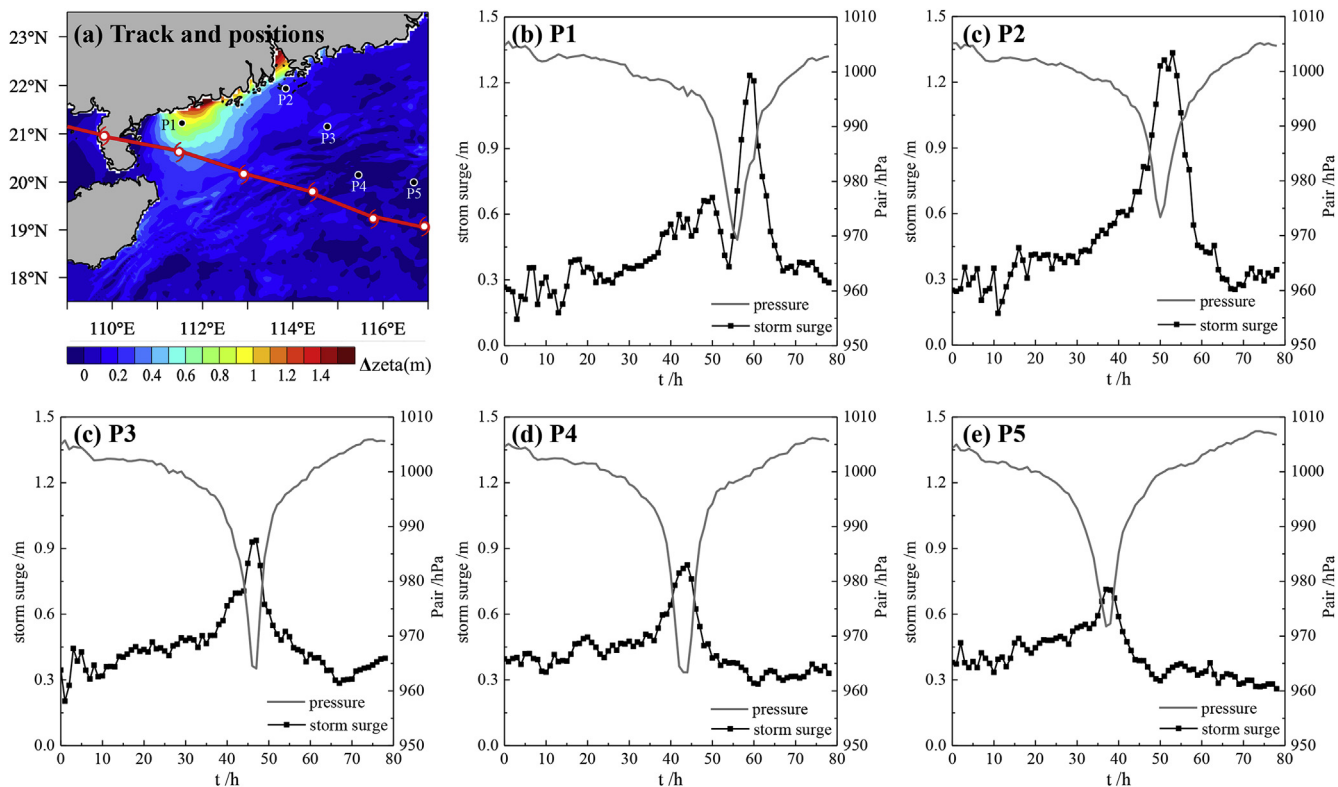


Fig. 14. Relationship between water level and pressure with time in each characteristic position (Start at 2012-08-15 00:00:00 UTC).

northern Philippines to the South China Sea as well as the process of the changing wind field and pressure field. The arrows in the figure indicates the speed vector at 10 m and the color indicates the pressure value.

As can be seen from the figure, after the Kai-tak moved to the South China Sea region, the cyclonic wind field had significantly increased, and the wind speed was always maintained above 30 m/s. After landing in Guangdong, the wind field strength rapid declined. From the spatial

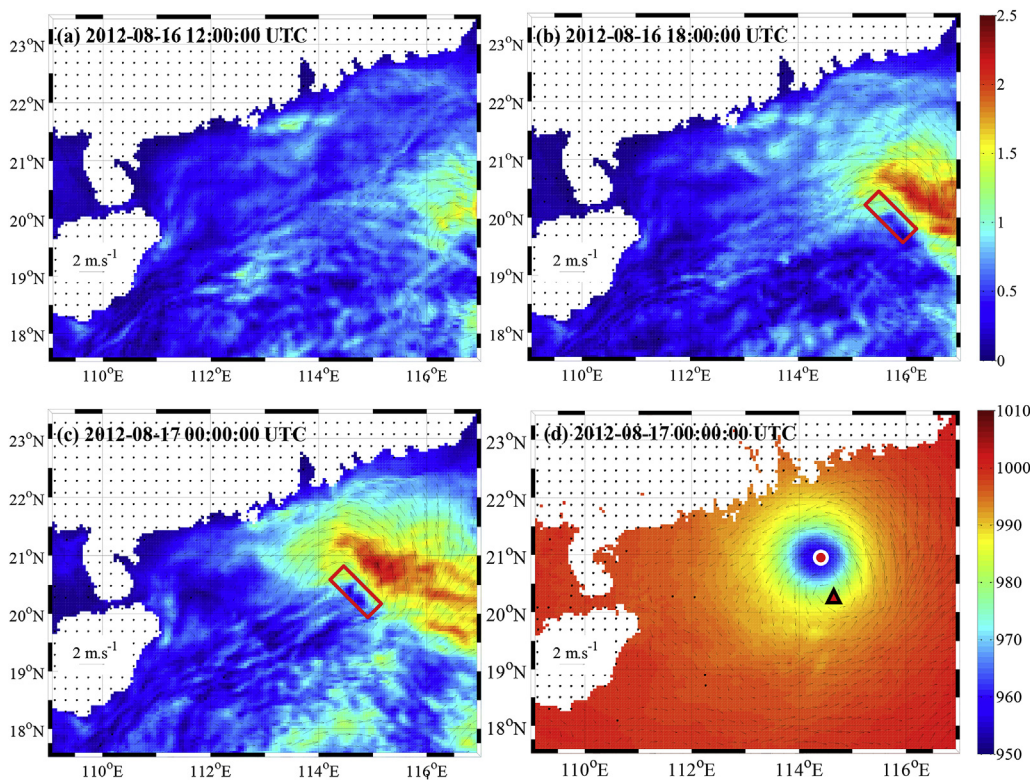


Fig. 15. The spatial distribution of flow field influenced by Typhoon Kai-tak. Arrow is the flow field; background color in (a)–(c) is the flow velocity (unit: m/s); background color in (d) is sea level pressure (unit: hPa). (For interpretation of the references to color in this figure legend, the reader is referred to the Web version of this article.)

distribution of the wind field, the wind speed on the right side of the typhoon center is significantly greater than the wind speed on the left side, which is due to the influence of Coriolis force.

It can also be seen in Fig. 10 that the pressure of the typhoon center was significantly reduced during the process of moving northwest after Typhoon Kai-tak entered the South China Sea from the northern Philippines. At 6:00 on August 16, the typhoon center pressure was less than 980 hPa. During the typhoon movement, the pressure in the center of the typhoon continued to decrease, and the minimum was less than 970 hPa. The pressure in the center of the typhoon began to rapidly rise after making landfall. From the figure, it can be seen that the center of the typhoon wind field is basically consistent with the center of the pressure field. The only exception in the pressure gradient on the right side of the track is larger than the left side, and the spatial distribution of the pressure field along the typhoon track is relatively symmetrical.

The shear stress at the sea-air interface due to the strong rotation of the air during the influence of typhoon is one of the important relationships between within the sea-air interaction. Fig. 11 shows the spatial distribution of the shear stress components in the latitude direction (surface u-momentum stress) and longitude direction (surface v-momentum stress) over the north of the South China Sea during the impact of the Typhoon Kai-tak. At 12:00 on the August 16, 2012, the shear stress was about 3 N/m^2 in the latitude direction and slightly larger at the longitude direction is about 4 N/m^2 . With the development of the typhoon, the intensity of typhoon increased. At 00:00 on August 17, 2012, the shear stress of the sea surface in the latitude direction increased to 4 N/m^2 or more, and the surface v-momentum stress increased to 5 N/m^2 .

4.2. Storm surge

Fig. 12 shows the change of water level in the north of the South China Sea under the influence of Typhoon Kai-tak in the coupled WRF-ROMS model. To facilitate comparison, the water level at each time is subtracted from the astronomical tide level before the typhoon is affected to obtain the results of storm surge under the influence of the

Typhoon Kai-tak, as shown in Fig. 13.

It can be seen from Fig. 13 that starting from 00:00 on August 16, 2012, under the influence of the Typhoon Kai-tak, the northern South China Sea region began to produce a higher storm surge. With the development of Typhoon Kai-tak, the water level of storm surge will increase. At the southwest coast of the Pearl River Estuary, the maximum level of the storm surge will be more than 1.5m. The increased water level on the right side of the typhoon track is greater than that on the left side, and the spatial distribution of the storm surge is asymmetrical.

To further analyze the water level change process of storm surge, five characteristic positions were selected near the track of Typhoon Kai-tak and the Pearl River Estuary, as shown in Fig. 14(a), to record the changes in the water level. Fig. 14(b–f) show the evolution of storm surge and typhoon pressure over time for each characteristic position. From the figure, it can be seen that the time with the maximum value of water level at each characteristic position is synchronized with the time of minimum value of the central pressure, and no time lag is shown.

4.3. Flow field

The strong rotating wind field formed by the typhoon above the sea surface will produce a clear wind-flow at the sea surface. Fig. 15 shows the flow field of the sea surface in the South China Sea during the impact of Typhoon Kai-tak. As can be seen from the figure, due to the impact of Typhoon Kai-tak, the surface currents in the South China Sea have undergone significant changes. On the sea surface, the left side of the typhoon track forms a clear low-velocity choke zone (red wireframe in Fig. 15(b and c)) with a flow velocity of less than 0.2 m/s and a local flow velocity even smaller. A large horizontal flow velocity is generated on both sides of the choke zone, and the direction is opposite. The flow velocity on the right side is about twice as large as that on the left side. The maximum flow velocity on the right side reaches 2.0 m/s , which is generated in the tail region of the right rear side of the typhoon. The maximum flow velocity on the left side is about 0.8 m/s . The local flow choke zone is divided into two sides by the boundary line and produced

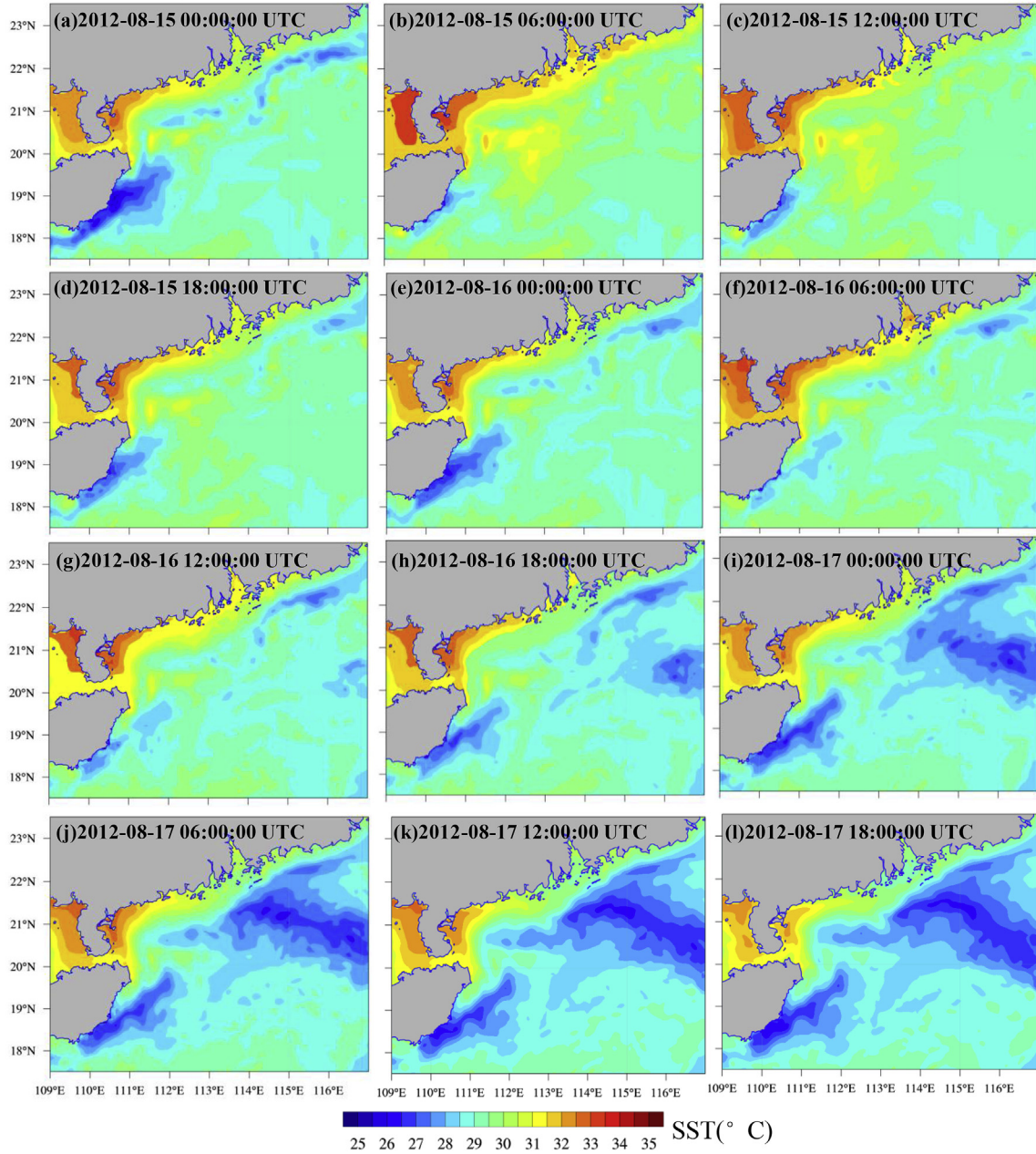


Fig. 16. Spatial distribution of SST influenced by the Typhoon Kai-tak.

a clear counterclockwise circulation field near the center of the typhoon.

From Fig. 15(a–c), it can be seen that the flow velocity on the right side in the circulation flow field is stronger than the flow velocity on the left side, that is, the flow field has an asymmetric distribution. Fig. 15(d) shows the spatial distribution of pressure at the same time. The circle is the center of the typhoon and the triangle represents the center of the circulation flow field. As can be seen from the figure, the center of the flow field is located at the right rear of the typhoon center, and the maximum flow velocity is also located at the right rear of the center of the typhoon. Therefore, the wind flow field has significant lag time.

4.4. Sea surface temperature

The sea surface temperature (SST) will be significantly reduced under the influence of the typhoon. Fig. 16 shows the evolution of SST

in the South China Sea by the coupled WRF-ROMS model during the impact of Typhoon Kai-tak. Fig. 17 shows the change variation distribution of the sea surface temperature in the South China Sea relative to that before the typhoon, which is the reference time at 00:00 on August 15, 2012.

As can be seen from Fig. 17, at 06:00 on the August 15, 2012 (UTC), the surface water is receiving external heat from factors such as solar radiation, resulting in an increase in sea surface temperature, where the sea surface temperature of the nearshore has increased by 4 °C before the Typhoon Kai-tak. From 12:00 on the August 15 (UTC), sea surface temperature began to cool. At 00:00 on August 16, 2012, due to the impact of the Typhoon Kai-tak, the temperature of the sea surrounding the typhoon center dropped significantly, and the maximum temperature dropped more than 4 °C.

The reduction of sea surface temperature under the influence of typhoon shows a clear asymmetrical distribution, that is, the temperature drop on the right side of the typhoon track is significantly

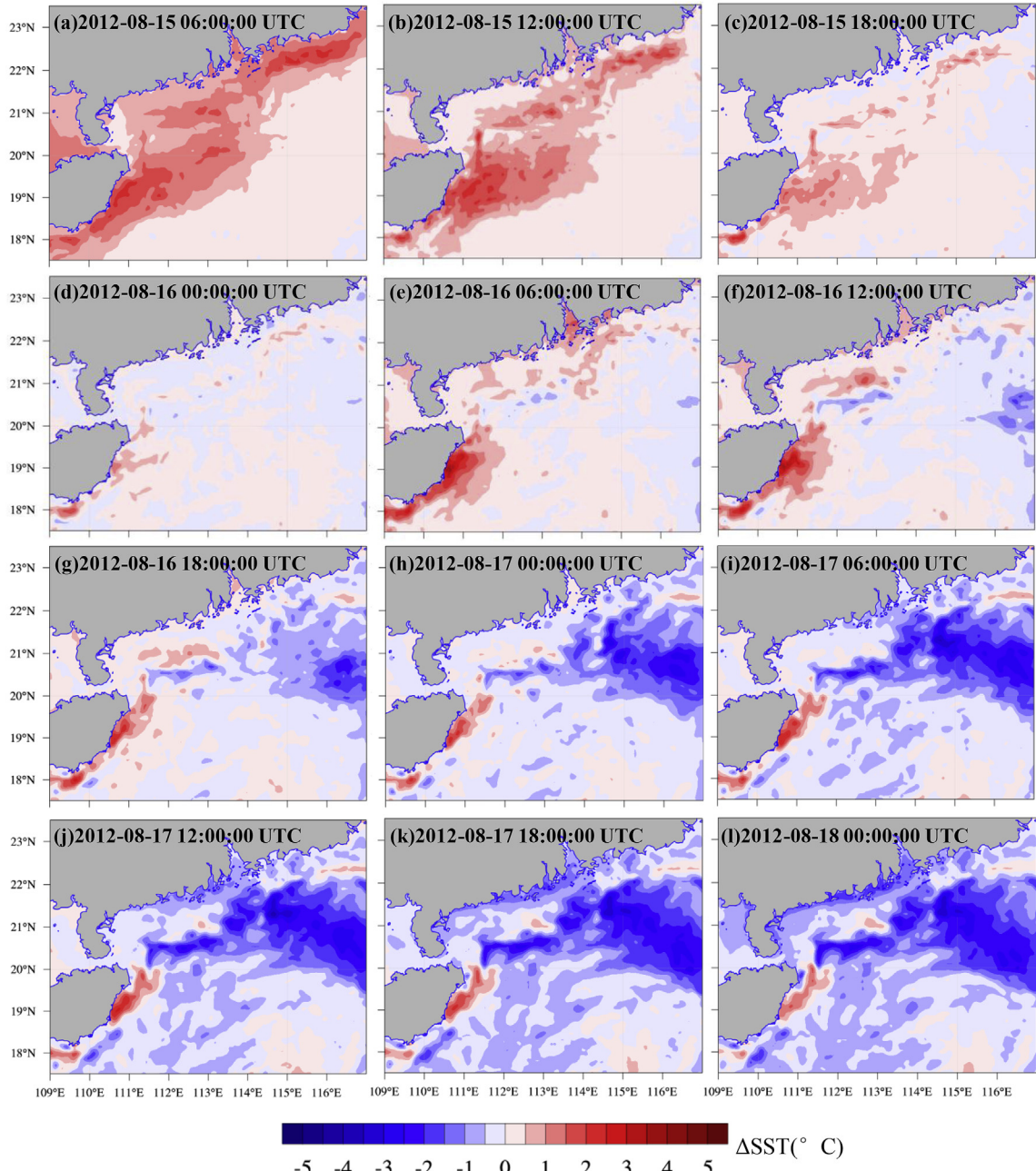


Fig. 17. Spatial distribution of ΔSST influenced by the Typhoon Kai-tak.
(reference time: 2012-08-15 00:00:00 UTC).

larger than that on the left side. As can be seen from Fig. 17, the temperature in the right side of the typhoon track can be cooled to more than 4°C , while the temperature in the left side of the typhoon track is about 2°C .

To further analyze the changing characteristic of SST under the influence of typhoon, as shown in Fig. 18(a), five characteristic positions were selected around the typhoon track, and the sea surface, middle and bottom temperature and local pressure changes over time were plotted in Fig. 18(b–f). At the initial stage of the typhoon impact, due to the influence of solar radiation and other factors on the sea water, heat transfer was performed with the outside, resulting in a cyclical rise and fall in sea surface temperature, especially in the nearshore positions (P1 and P2), Fig. 18 (b) and (c) are shown in red dashed wireframes.

The sea surface temperature in each characteristic position has

dropped and was affected by the typhoon. In the deep-sea positions (P3, P4 and P5), the sea surface temperature has dropped by more than 3°C , and the sea surface temperature in nearshore positions (P1 and P2) has dropped by more than 1°C . This is due to the fact that under the influence of typhoon, the strong mixing in the typhoon process results in large velocity shear at the bottom of the ocean mixed layer. The cool water located in the lower layer of the ocean rises and become upwelling under the influence of pumping. The cool water and the upper layer warm water mixing causes the temperature of the mixed layer water to cool. In terms of time, the decrease of the seawater temperature delays behind the moment when the atmospheric pressure extreme occurs, that is, the seawater temperature has a time lag in response to the typhoon.

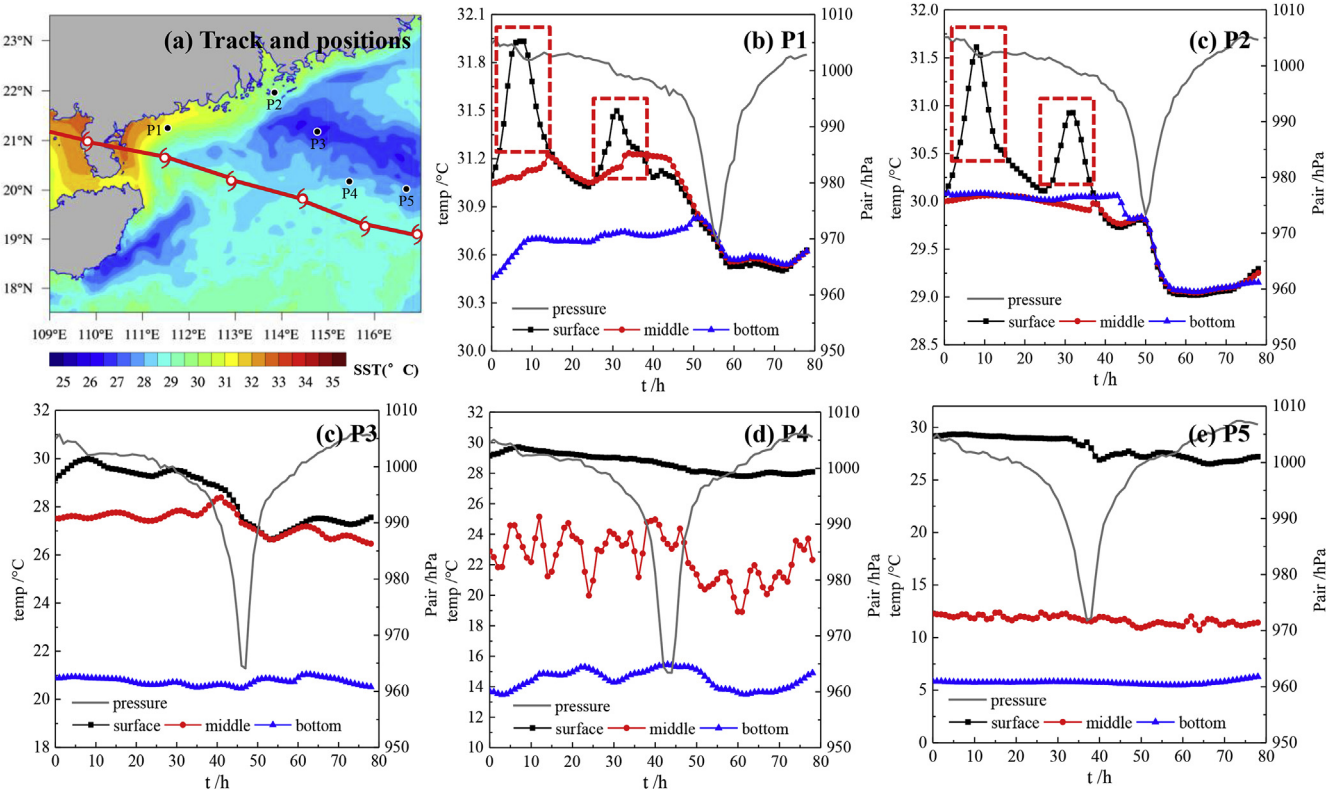


Fig. 18. The variability of sea temperature in different layers and different positions.
(Start at 2012-08-15 00:00:00 UTC).

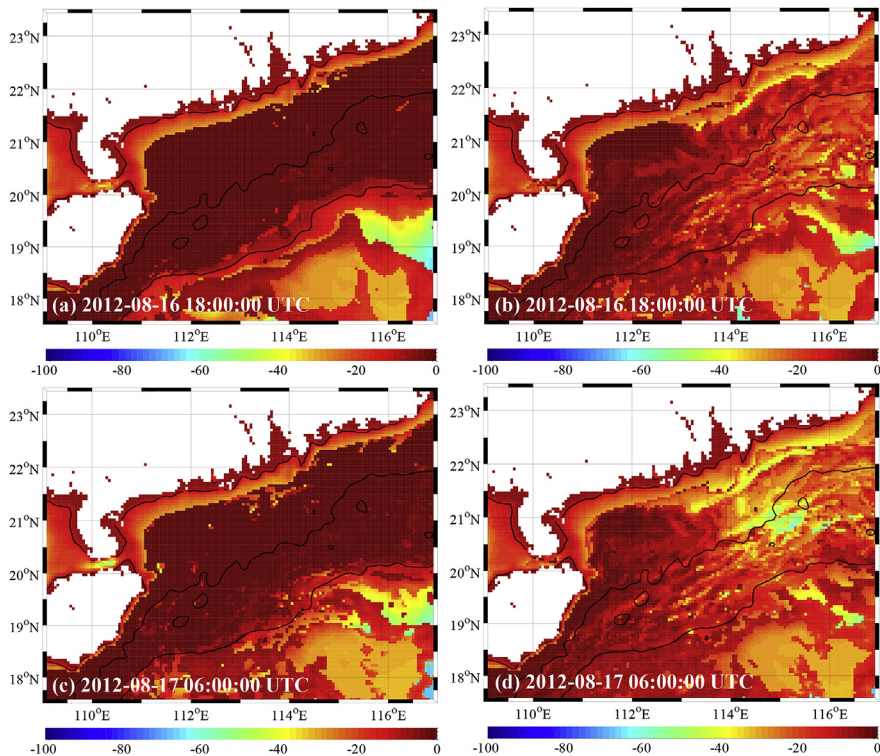


Fig. 19. Spatial distribution of the MLD by Lorbacher's method (unit: m).
Left is the results in Exp-ROMS and right is the results in Exp-CWR.

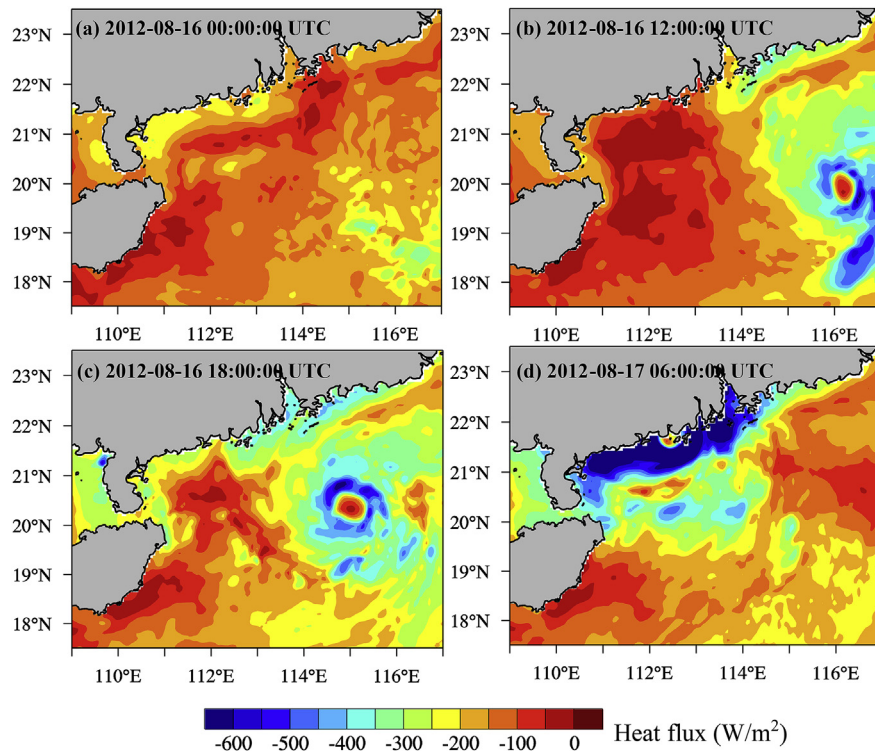


Fig. 20. Spatial distribution of latent heat flux influenced by Typhoon Kai-tak.

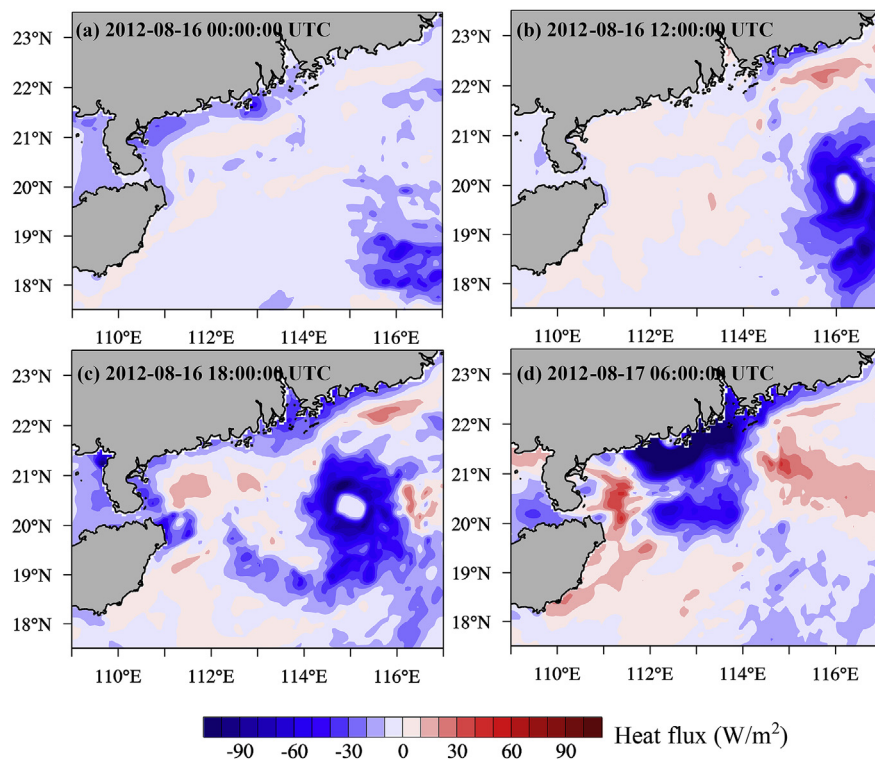


Fig. 21. Spatial distribution of sensible heat flux influenced by Typhoon Kai-tak.

4.5. Mixed layer depth

During the impact of typhoon, the depth of ocean mixed layer (mixed layer depth, MLD) will change significantly. Fig. 19 shows the results of the mixed layer depth based on the two experiments respectively, Exp-ROMS (only ROMS model) and the Exp-CWR (coupled WRF-

ROMS model). The mixed layer depth is calculated using the method by Lorbacher et al. (2006). In Exp-ROMS, the mixed layer depth under the forcing condition from the astronomical tide during Typhoon Kai-tak was calculated, while in the Exp-CWR, the mixed layer depth under influence of Typhoon Kai-tak was calculated using the coupled atmosphere-ocean model.

As can be seen from Fig. 19, the distribution of mixed layer depth under the influence of the astronomical tide at different times is relatively stable. Due to the influence of tides and coastal ocean currents in the nearshore, the mixed layer depth can reach about 10 m; outside the 1000 m isobath, the mixed layer depth can reach about 60 m due to the larger depth of the water.

In the experiment of the coupled WRF-ROMS model, the spatial distribution of the mixed layer depth under the influence of Typhoon Kai-tak changed significantly. It can be seen from the figure that the mixed layer depth in the coupled WRF-ROMS model under the influence of the typhoon is significantly greater than the mixed layer depth under the influence of the astronomical tide. Because the typhoon caused a strong vortex shedding force and triggered a strong Ekman pumping, the mixed layer depth near the typhoon track was large. In the region within 100 m isobath, the mixed layer depth can reach more than 60 m, and that means almost all water in this region is mixed influenced by the typhoon.

4.6. Heat fluxes

Heat flux is an important method for heat exchange between the atmosphere and the ocean during a typhoon, which is divided into latent heat and sensible heat. Latent heat flux is the release of latent heat due to the vaporization of water vapor, which is the heat generated by vaporization of water vapor from the ocean surface, and the value of latent heat flux is negative. Sensible heat flux is the heat exchange generated due to the temperature difference of sea and air, and the value of sensible heat flux can be positive or negative. A positive value indicates that the ocean transfers heat to the atmosphere, and a negative value indicates that the atmosphere transfers heat to the ocean.

Fig. 20 shows the spatial distribution of the latent heat flux obtained by the coupled WRF-ROMS model at different times in the northern South China Sea during Typhoon Kai-tak. It can be seen from the figure that the extremum position of latent heat flux occurs near the center of the typhoon and can reach about -500 W/m^2 . In the nearshore region, the latent heat flux when the typhoon is landing can exceed -600 W/m^2 .

Fig. 21 shows the results of the sensible heat flux distribution at the corresponding time under the same conditions in the northern South China Sea during Typhoon Kai-tak. It can be seen from the figure that the extremum position of the sensible heat flux also appears near the center of the typhoon and is a negative value, which is about -100 W/m^2 . In the center of the typhoon center and 100 km around the center, the sensible heat flux is positive, and the sensible heat flux of 100 km around the center of the typhoon center is about 50 W/m^2 .

Through the comparison of latent heat flux and sensible heat flux, it can be seen that the heat exchange at the sea-air interface comes primarily from latent heat during the impact of Typhoon Kai-tak. The heat exchange at the air-sea interface is very strong under the influence of typhoon. The latent heat generated by water vapor evaporation plays a dominant role in the heat exchange at the air-sea interface, which shows that the heat carried by the vaporization of the sea surface is one of the important factors for the decrease of seawater temperature under the influence of the typhoon.

5. Conclusions

A coupled atmosphere-ocean model in the South China Sea was established based on the mesoscale atmospheric model WRF and the regional ocean model ROMS. The GSHHS shoreline data and the ETOPO1 depth data have been used in this model. The harmonic constants of the ROMS model are derived from the OTIS model provided from Oregon State University. The surface stress, sensible heat flux, latent heat flux, shortwave radiation flux, and longwave radiation flux calculated by WRF and delivered to ROMS through MCT. While the SST calculated by ROMS is feedback to the WRF through MCT.

Based on the two-way coupled WRF-ROMS model, the atmosphere and ocean dynamics in the South China Sea induced by Typhoon Kai-tak has been calculated, and the relationship between sea-air interaction has been analyzed. The typhoon track, intensity, and strength have been calculated from the coupled model and are compared with the observation results. The verification results show that the typhoon track error is controlled within a range of 60 km, and the calculated typhoon intensity and strength is slightly larger than the observation result.

From the spatial distribution of the wind field, the wind speed, air pressure and wind-driven flow field on the right side of the typhoon center is significantly stronger than the left side, which is due to the influence of Coriolis force. Wind-driven flow field has obvious lag in time. Sea surface temperature has an asymmetrical distribution in space and has lag in time. The heat exchange at the air-sea interface is very strong under the influence of typhoon. The latent heat generated by water vapor evaporation plays a dominant role in the heat exchange at the air-sea interface.

Acknowledgments

The study was supported by the National Natural Science Foundation of China (Grant Nos. 51809023, 51879015, 51839002 and 51809021). The Partial Support also comes from the Open Research Foundation of the Key Laboratory of the Pearl River Estuarine Dynamics and Associated Process Regulation, the Ministry of Water Resources (No. 2018KJ03), the Key Laboratory of Water-Sediment Sciences and Water Disaster Prevention of Hunan Province (No. 2017SS04) and Key Laboratory of Technology for Safeguarding of Maritime Rights and Interests and Application, SOA (No. SCS1606). The authors are grateful to the anonymous reviewers for their valuable input.

References

- Black, P.G., D'Asaro, E.A., Sanford, T.B., et al., 2007. Air-sea exchange in hurricanes: synthesis of observations from the coupled boundary layer air-sea transfer experiment. *Bull. Am. Meteorol. Soc.* 88 (3), 357–374.
- Blumberg, A.F., Georgas, N., Yin, L., et al., 2015. Street-scale modeling of storm surge inundation along the New Jersey Hudson river waterfront. *J. Atmos. Ocean. Technol.* 32 (8), 1486–1497.
- Blumberg, A.F., Mellor, G.L., 1987. A Description of a Three-Dimensional Coastal Ocean Circulation model[C]. *Three-Dimensional Coastal Ocean Models*, Washington, USA. pp. 1–16.
- Chia, H.H., Ropelewski, C.F., 2002. The interannual variability in the genesis location of tropical cyclones in the northwest Pacific. *J. Clim.* 15 (20), 2934–2944.
- Chen, T., Zhang, Q., Wu, Y., et al., 2018. Development of a wave-current model through coupling of FVCOM and SWAN. *Ocean Eng.* 164, 443–454.
- Chen, S., Qian, Y.K., Peng, S., 2015. Effects of various combinations of boundary layer schemes and microphysics schemes on the track forecasts of tropical cyclones over the South China Sea. *Nat. Hazards* 78 (1), 61–74.
- Craig, A.P., Jacob, R., Kauffman, B., et al., 2005. CPL6: the new extensible, high performance parallel coupler for the Community Climate System Model. *Int. J. High Perform. Comput. Appl.* 19 (3), 309–327.
- Di, Liberto T., Colle, B.A., Georgas, N., et al., 2011. Verification of a multimodel storm surge ensemble around New York City and Long Island for the cool season. *Weather Forecast.* 26 (6), 922–939.
- Forbes, C., Rhome, J., Mattocks, C., et al., 2014. Predicting the storm surge threat of hurricane sandy with the national weather service SLOSH model. *J. Mar. Sci. Eng.* 2 (2), 437–476.
- Ge, Z., Dai, Z., Pang, W., et al., 2017. LIDAR-based detection of the post-typhoon recovery of a meso-macro-tidal beach in the Beibu Gulf, China. *Mar. Geol.* 391, 127–143.
- Gronholz, A., Gräwe, U., Paul, A., et al., 2017. Investigating the effects of a summer storm on the North Sea stratification using a regional coupled ocean-atmosphere model. *Ocean Dynam.* 67 (2), 1–25.
- Haidvogel, D.B., Arango, H., Budgell, W.P., et al., 2008. Ocean forecasting in terrain-following coordinates: formulation and skill assessment of the regional ocean modeling system. *J. Comput. Phys.* 227 (7), 3595–3624.
- Hu, D., Wu, L., Cai, W., et al., 2015a. Pacific western boundary currents and their roles in climate. *Nature* 522 (7556), 299.
- Hu, K., Chen, Q., Wang, H., 2015b. A numerical study of vegetation impact on reducing storm surge by wetlands in a semi-enclosed estuary. *Coast. Eng.* 95, 66–76.
- Islam, T., Srivastava, P.K., Rico-Ramirez, M.A., et al., 2015. Tracking a tropical cyclone through WRF-ARW simulation and sensitivity of model physics. *Nat. Hazards* 76 (3), 1473–1495.
- Jiang, C., Wu, Z., Chen, J., et al., 2017. An available formula of the sandy beach state

- induced by plunging waves. *Acta Oceanol. Sin.* 36 (9), 91–100.
- Jelesnianski, C.P., Chen, J., Shaffer, W.A., 1992. SLOSH: Sea, Lake, and Overland Surges from hurricanes. National Weather Service, USA.
- Jones, P.W., 1998. A Users Guide for SCRIP: A Spherical Coordinate Remapping and Interpolation Package. Los Alamos National Laboratory. <http://climate.lanl.gov/Software/SCRIP/>.
- Lakshmi, D.D., Murty, P.L.N., Bhaskaran, P.K., et al., 2017. Performance of WRF-ARW winds on computed storm surge using hydrodynamic model for Phailin and Hudhud cyclones. *Ocean. Eng.* 131, 135–148.
- Laprise, R., 1992. The Euler equations of motion with hydrostatic pressure as an independent variable. *Mon. Weather Rev.* 120 (1), 197–207.
- Lee, T.L., 2006. Neural network prediction of a storm surge. *Ocean. Eng.* 33 (3–4), 483–494.
- Li, M., Zhong, L., Boicourt, W.C., et al., 2006. Hurricane-induced storm surges, currents and destratification in a semi-enclosed bay. *Geophys. Res. Lett.* 33 (2).
- Li, Y., Peng, S., Yan, J., et al., 2013. On improving storm surge forecasting using an adjoint optimal technique. *Ocean Model.* 72, 185–197.
- Liu, B., Liu, H., Xie, L., et al., 2010. A coupled atmosphere-wave-ocean modeling system: simulation of the intensity of an idealized tropical cyclone. *Mon. Weather Rev.* 139 (1), 132–152.
- Liu, D., Pang, L., Xie, B., 2009. Typhoon disaster in China: prediction, prevention, and mitigation. *Nat. Hazards* 49 (3), 421–436.
- Liu, N., Ling, T., Wang, H., et al., 2015. Numerical simulation of typhoon Muifa (2011) using a coupled ocean-atmosphere-wave-sediment transport (COAWST) modeling system. *J. Ocean Univ. China* 14 (2), 199–209.
- Lorbacher, K., Dommenget, D., Niiler, P.P., et al., 2006. Ocean mixed layer depth: a subsurface proxy of ocean-atmosphere variability. *Journal of Geophysical Research Oceans* 111 (C7), 520–522.
- Mattocks, C., Forbes, C., 2008. A real-time, event-triggered storm surge forecasting system for the state of North Carolina. *Ocean Model.* 25 (3–4), 95–119.
- Mei, X., Dai, Z., Darby, S.E., et al., 2018. Modulation of extreme flood levels by impoundment significantly offset by floodplain loss downstream of the Three Gorges Dam. *Geophys. Res. Lett.* 45 (7), 3147–3155.
- Mooney, P.A., Mulligan, F.J., Bruyère, C.L., et al., 2019. Investigating the performance of coupled WRF-ROMS simulations of Hurricane Irene (2011) in a regional climate modeling framework. *Atmos. Res.* 215, 57–74.
- Mori, N., Kato, M., Kim, S., et al., 2014. Local amplification of storm surge by super typhoon Haiyan in Leyte Gulf. *Geophys. Res. Lett.* 41 (14), 5106–5113.
- Neumann, J.E., Emanuel, K., Ravela, S., et al., 2015. Joint effects of storm surge and sea-level rise on US Coasts: new economic estimates of impacts, adaptation, and benefits of mitigation policy. *Climatic Change* 129 (1–2), 337–349.
- Pattanayak, S., Mohanty, U.C., Rao, A.D., 2016. Simulation of storm surges in the bay of Bengal using one-way coupling between NMM-WRF and IITD storm surge model. *Mar. Geodes.* 39 (5), 376–400.
- Rego, J.L., Li, C., 2010. Nonlinear terms in storm surge predictions: effect of tide and shelf geometry with case study from Hurricane Rita. *J. Geophys. Res.: Oceans* 115 (C6).
- Sebastian, A., Proft, J., Dietrich, J.C., et al., 2014. Characterizing hurricane storm surge behavior in Galveston Bay using the SWAN+ ADCIRC model. *Coast. Eng.* 88, 171–181.
- Sheng, Y.P., Alymov, V., Paramygin, V.A., 2010. Simulation of storm surge, wave, currents, and inundation in the Outer Banks and Chesapeake Bay during Hurricane Isabel in 2003: the importance of waves. *J. Geophys. Res.: Oceans* 115 (C4).
- Sun, J., Wang, G., Zuo, J., et al., 2017. Role of surface warming in the northward shift of tropical cyclone tracks over the South China Sea in November. *Acta Oceanol. Sin.* 36 (5), 67–72.
- Takagi, H., Esteban, M., Shibayama, T., et al., 2017. Track analysis, simulation, and field survey of the 2013 Typhoon Haiyan storm surge. *Journal of Flood Risk Management* 10 (1), 42–52.
- Vu, T., Lam, N., 2005. A simulation model for storm surge along Vietnamese coast. *Journal of Water Resources & Environmental Engineering* 1 (9), 68–74.
- Wang, G., Su, J., Ding, Y., et al., 2007. Tropical cyclone genesis over the south China sea. *J. Mar. Syst.* 68 (3–4), 318–326.
- Wang, J., Yi, S., Li, M., et al., 2018. Effects of sea level rise, land subsidence, bathymetric change and typhoon tracks on storm flooding in the coastal areas of Shanghai. *Sci. Total Environ.* 621, 228–234.
- Wang, Z., Zhou, L., Li, Q., et al., 2017. Storm surge along the yellow river delta under directional extreme wind conditions. *J. Coast Res.* 80 (sp1), 86–91.
- Wang, Z.L., Lu, Y.J., Geng, Y.F., 2010. Derivation of parametric tropical cyclone models for storm surge modeling. *China Ocean Eng.* 24 (2), 245–254.
- Warner, J.C., Sherwood, C.R., Signell, R.P., et al., 2008. Development of a three-dimensional, regional, coupled wave, current, and sediment-transport model. *Comput. Geosci.* 34 (10), 1284–1306.
- Warner, J.C., Armstrong, B., He, R., et al., 2010. Development of a coupled ocean-atmosphere-wave-sediment transport (COAWST) modeling system. *Ocean Model.* 35 (3), 230–244.
- Weisberg, R.H., Zheng, L., 2006. Circulation of Tampa Bay driven by buoyancy, tides, and winds, as simulated using a finite volume coastal ocean model. *J. Geophys. Res.: Oceans* 111 (C1).
- Wu, Z., Jiang, C., Chen, J., et al., 2019. Three-Dimensional temperature field change in the south China Sea during typhoon Kai-tak (1213) based on a fully coupled atmosphere-wave-ocean model. *Water* 11 (1), 140.
- Wu, Z., Jiang, C., Deng, B., et al., 2018. Evaluation of numerical wave model for typhoon wave simulation in South China Sea. *Water Science and Engineering* 11 (3), 229–235.
- Xie, L., Pietrafesa, L.J., Peng, M., 2004. Incorporation of a mass-conserving inundation scheme into a three dimensional storm surge model. *J. Coast Res.* 1209–1223.
- Xie, S.P., Kosaka, Y., Du, Y., et al., 2016. Indo-western Pacific ocean capacitor and coherent climate anomalies in post-ENSO summer: a review. *Adv. Atmos. Sci.* 33 (4), 411–432.
- Yang, J., Sato, M., Liu, N., et al., 2018. A gigantic jet observed over an mesoscale convective system in midlatitude region. *J. Geophys. Res.: Atmosphere* 123 (2), 977–996.
- Yang, X., Haas, K.A., 2015. Improving assessments of tidal power potential using grid refinement in the Coupled Ocean-Atmosphere-Wave-Sediment Transport model. *J. Renew. Sustain. Energy* 7 (4), 21–27.
- Yang, X., Zhang, Q., Zhang, J., et al., 2015. An integrated model for three-dimensional cohesive sediment transport in storm event and its application on Lianyungang Harbor, China. *Ocean Dynam.* 65 (3), 395–417.
- Yin, K., Xu, S., Huang, W., et al., 2017. Effects of sea level rise and typhoon intensity on storm surge and waves in Pearl River Estuary. *Ocean. Eng.* 136, 80–93.
- You, S.H., Lee, W.J., Moon, K.S., 2010. Comparison of storm surge/tide predictions between a 2-D operational forecast system, the regional tide/storm surge model (RTSM), and the 3-D regional ocean modeling system (ROMS). *Ocean Dynam.* 60 (2), 443–459.
- Zambon, J.B., He, R., Warner, J.C., 2014. Investigation of hurricane Ivan using the coupled ocean-atmosphere-wave-sediment transport (COAWST) model. *Ocean Dynam.* 64 (11), 1535–1554.
- Zhang, K., Li, Y., Liu, H., et al., 2013. Transition of the coastal and estuarine storm tide model to an operational storm surge forecast model: a case study of the Florida coast. *Weather Forecast.* 28 (4), 1019–1037.
- Zhang, Y., Baptista, A.M., 2008. SELFE: a semi-implicit Eulerian-Lagrangian finite-element model for cross-scale ocean circulation. *Ocean Model.* 21 (3–4), 71–96.